

Quasi Normal Modes of hairy black holes at higher-order WKB approach.

R. Avalos^{a,1}, E. Contreras^{b,1}

¹ Departamento de Física, Colegio de Ciencias e Ingeniería, Universidad San Francisco de Quito, Quito, Ecuador.

Received: date / Accepted: date

Abstract In this work, we implement the 13th order semi-analytical WKB method to explore the stability of hairy black holes obtained in the framework of Gravitational Decoupling. In particular, we perform a detailed analysis of the frequencies of the quasi-normal modes as a function of the primary hair of the solutions with the aim to bound their values. We explore a broad interval in a step of 0.1 of the hair parameters. We find that except for some cases where the method is expected to have poor accuracy, all the solutions seem to be stable and the role played by the primary hair is twofold: to modulate the damping factor of the perturbation and to decrease the frequency of its oscillation.

1 Introduction

Although non-hair conjecture states that black holes (BH) are the simplest objects in nature described only by a few parameters, namely its mass, charge, and angular momentum, a real BH is far from being isolated. Indeed, black holes are surrounded by galactic nuclei, stars, planets, etc, so they are always in a perturbed state [1]. In this regard, to analyze the stability of BH's we have to start with the study of their perturbation.

For the study of how a BH responds to perturbation, we can consider either perturbing the BH background (the spacetime metric) or adding extra fields to the BH spacetime. In any case, the equation describing the perturbation of the BH reduces to a radial like-Shrödinger equation in which complex frequencies solutions correspond to the quasinormal modes (QNM) of the BH. More precisely, the real part of the QNM

frequencies, $Re(\omega)$, corresponds to the frequency of oscillations, and the imaginary part, $Im(\omega)$, is related to the damping factor associated with the loss of energy through gravitational radiation. It is worth mentioning that if $Im(\omega) > 0$ the perturbation grows exponentially leading to instabilities in the system so that a stable solution will be that which $Im(\omega) < 0$.

The computation of the QNM modes can be performed through a variety of methods (for an incomplete list see [2–18] and references therein, for example). However, in this work, we shall use the recently developed WKB approximation to the 13th order which has brought the attention of the community [19]. It should be emphasized that as the computation of QNM modes can only be performed semi-analytically, the set of any free parameter appearing in the BH solution is compulsory. As a consequence, the computation of QNM modes allows the definition of the parameter space of any solution by demanding $Im(\omega) < 0$. This strategy has been applied in Ref. [20] with the aim to bound the free parameters in the construction of stable traversable wormholes.

In this work, we explore the stability through the computation of the QNM by the 13th order WKB method of hairy black holes obtained by Gravitational decoupling in Ref. [21]. The main goal is to bound in the values taken by the “primary” hairs of the solution. It is worth mentioning that, during the writing of this work, there have been reported two independent studies on the QNM modes for the same models [22, 23]. However, in our analysis, we make an extensive study on the frequencies as a function of the primary hairs of the solution that has not been reported before.

This work is organized as follows. In the next section, we review the main aspects related computation of the QNM associated to perturbation of a BH. In sec-

^ae-mail: ravalos@usfq.edu.ec

^be-mail: econtreras@usfq.edu.ec

tion 3, we introduce the hairy BH models in which we base our analysis. Section 4 is devoted to the analysis of the results obtained and in the last section we conclude the work.

2 QNM by the WKB approximation

Let us consider a static and spherically symmetry line element satisfying the Schwarzschild condition, namely

$$ds^2 = f(r)dt^2 - \frac{dr^2}{f(r)} - r^2(d\theta^2 + \sin^2\theta d\phi^2), \quad (1)$$

with $f(r)$ the so-called lapse function encoding the information of the BH spacetime. Next, the perturbation of the BH can be performed by adding test fields (Klein-Gordon or Dirac fields) to the background or by perturbing the spacetime itself. In any case, the perturbation equation can be reduced to a like-Schrödinger equation of the form

$$\left(\frac{d^2}{dr_*^2} + \omega^2 - V(r_*)\right)\chi(r_*) = 0, \quad (2)$$

where r_* is the tortoise radial coordinates

$$\frac{dr_*}{dr} = \frac{1}{f(r)}, \quad (3)$$

and $V(r)$ is an effective potential, which for axial perturbations takes the form

$$V_L(r) = f(r) \left(\frac{L(L+1)}{r^2} + f'(r) \frac{(1-s^2)}{r} \right), \quad (4)$$

where $s = 0, 1, 2$ is the spin of the perturbing field. In this work, we shall impose $s = 0$ (scalar field). Besides, ω represent the frequency of the QNM and has a real and an imaginary part, namely $\omega = \text{Re}(\omega) + i\text{Im}(\omega)$.

Several strategies can be implemented to obtain the QNM frequencies. However, in this work we shall implement the WKB approximation first introduced in Ref. [24] to study scattering around BH's, given its similarity with the one-dimensional Schrödinger equation with a potential barrier. Now, as the problem demands that both the “reflected” and “transmitted” waves of the scattering problem have comparable amplitudes, the problem reduces to implement the WKB method to high orders around the top of the potential. It can be shown that the 13th WKB order formula reads

$$i \frac{\omega^2 - V_0}{\sqrt{-2V_0''}} - \sum_{j=2}^{13} A_j = n + \frac{1}{2}, \quad (5)$$

where V_0 is the maximum height of the potential and V_0'' is its second derivative with respect to the tortoise coordinate evaluated at the radius where V_0 reaches a maximum. The values A_j are corrections that depend on the value of the potential and higher derivatives of it at the maximum. The exact expressions for the terms A_j are too long to be shown here but can be found in [19].

3 Hairy black holes

In this section we briefly describe the hairy black holes obtained in Ref. [21] by the Gravitational Decoupling (GD) through the Minimal Geometric Deformation (MGD) extended (for details about GD and MGD see [25–74]). As it is shown in [21], the solutions satisfy either the strong (SEC) and the dominant (DEC) energy conditions outside the horizon which make them attractive geometries in the modeling of suitable BH-hair systems.

3.1 Model 1

This black hole is characterized by a metric function of the form

$$f(r) = 1 - \frac{2M}{r} + \alpha \left(e^{-r/M} - \frac{2M}{r} e^{-2} \right), \quad (6)$$

where α is the decoupling parameter which connects (2) with the Schwarzschild black hole which is obtain in the limit $\alpha \rightarrow 0$. Note that the event horizon is located in $r_H = 2M$ which equals the Schwarzschild horizon. As can be seen in Ref. [21], this solution satisfies the SEC outside the horizon.

3.2 Model 2

In this case, the metric function takes the form

$$f(r) = 1 - \frac{2M}{r} + \left(1 + \frac{\alpha}{2e^2} \right) + \frac{4\alpha M^2}{e^2 r^2} - \frac{\alpha M}{r} e^{-r/M}, \quad (7)$$

As in the previous case, this solution reduces to the Schwarzschild BH when $\alpha = 0$. Besides, the horizon radius is located at $r_H = 2M$. As shown in Ref. [21], this solution satisfies the DEC outside the horizon.

3.3 Model 3

This black hole is characterized by a metric function of the form

$$f(r) = 1 - \frac{2M + \ell_0}{r} + \frac{2\ell_0 M}{r^2} - \frac{\alpha M e^{-r/M}}{r^2} \left(r - \ell_0 e^{\frac{r-\ell_0}{M}} \right), \quad (8)$$

and has the event horizon is in $r_H = \alpha\ell = \ell_0$, being ℓ a parameter that relates α and ℓ_0 . For the rest of the work we will fix $\ell = 1$ which means $\alpha = \ell_0$. This solution satisfies the DEC.

3.4 Model 4

This black hole is characterized by a metric function of the form

$$f(r) = 1 - \frac{2M + \ell_0}{r} - \frac{\alpha M e^{-r/M}}{r^2} \left(r - (2M + \ell_0) e^{\frac{r - (2M + \ell_0)}{M}} \right), \quad (9)$$

and has the event horizon is in $r_H = \alpha \ell = \ell_0$, being ℓ a parameter that relates α and ℓ_0 . For the rest of the work we will fix $\ell = 1$ which means $\alpha = \ell_0$. This solution satisfies the DEC.

Before concluding this section, a couple of comments are in order. First, it is worth mentioning that in [75] the geodesic analysis of the set of metric describing models 1-4 has been performed. In such a work, the authors not only studied the basic stuff related to the motion of massive and massless particles around the hairy black hole but they explored their potential as a mimickers of rotating black holes based on available data. This was achieved by comparing the radius of the innermost circular orbits (ISCO) of the static solution with that obtained from the Kerr solution. The relation between both ISCO radius was used to bound the values of the hairs as a function of the spin parameter of the rotating solution. The results obtained allow to consider the black holes described by the metrics here as mimickers of the systems ARK564 and NGC1365. The spin parameter of both systems was derived from relativistic reflection fitting of SMBH X-ray as reported in [76–78]. Second, the set of metric considered here was used as the seed for the construction of a rotating black hole by following the Gravitational Decoupling approach for stationary space-times [79]. Although in that work the shadow cast by this solution was found, an extensive analysis can be performed in order to compare the results with the EHT data. Indeed, we can use the strategy followed in [80] where the authors constraint Einstein-Yang-Mills parameter via frequency analysis of the quasi periodic normal oscillations and the EHT data of shadow cast by the M87 super massive BH. In the same direction, the results obtained in [79] based on the set of metric we are assuming in the present work, could be used to constraint the value of the hair associated with each of them. However, although this treatment is out of the scope of this work, we can estimate the typical size of the shadow, \mathcal{R}_s , of the M87 supermassive BH based on the set of the static metrics here as an approximation. To this end, we proceed as follows. First, the angular diameter of the BH shadow, θ_s , can be expressed as [80]

$$\theta_s = 2 \times 9.87098 \times 10^{-6} \mathcal{R}_s \left(\frac{M}{M_\odot} \right) \left(\frac{1 \text{ kpc}}{D} \right) \mu\text{as}, \quad (10)$$

where M and D are the mass and the distance of the BH, respectively. For the M87 BH, $\theta_s = (42 \pm 3) \mu\text{as}$, $M = 6.5 \times 10^9 M_\odot$ and $D = 16.8 \text{ Mpc}$ so that $\mathcal{R}_s = 5.49874$. Second, from [81, 82] it is known that the relationship between the shadow and the radius of the photon sphere r_0 is given by

$$\mathcal{R}_s = \frac{r_0}{f(r_0)} \quad (11)$$

with f the lapse function under consideration. The radius of the photon sphere of the metrics under consideration was obtained numerically and are shown in figure 7 of [75] for $\{\alpha, \ell_0\} \in (0, 3)$. Using this data in (1), we obtain \mathcal{R}_s as function of the primary hairs as is shown in Fig. 1. Note that, the model 2 is the only one that cannot be used to mimic the shadow of the M87 supermassive BH. It should be emphasized that comparison we are doing here must be taken as an approximation.

It is worth mentioning that the primary hairs, namely α in Models 1 and 2 and ℓ_0 in Models 3 and 4, can take arbitrary values in principle. For example, in Refs. [21, 75] we have taken $\{\alpha, \ell_0\} \in (0, 1)$. In this work we explore the stability of the solution in a larger interval. Although we have studied the behaviour for $\alpha, \ell_0 \in (-50, 50)$, here we show the results in the interval $(-10, 10)$ given that, essentially, it contains all the information we require.

4 Results and Discussion

In this section, we shall discuss the results obtained by the implementation of the WKB method in the models described in the previous sections. In all of the cases have plotted $\text{Im}(\omega)$ as a function of the primary hair of the BH with the aim to explore if there is a change in the imaginary part of the frequency for some of their values. All the results are shown in Figs. (2), (3), (4) and (5) for Models 1, 2, 3 and 4 respectively. All the computations have been performed setting the multipole number L and varying the overtone $n = 0, 1, 2, 3, 4$. For each model we have a plot for each $L = 2, 3, 4, 5, 6, 7, 8, 9, 10$. It is worth mentioning that in all the plots we have taken a step of 0.1 for the hair parameters, namely α, ℓ_0 . Higher precision is possible but the computational time increases considerably.

In Fig. 2 for $L = 2$, we note an increasing in the value of $\text{Im}(\omega)$ and then an oscillatory behaviour around $\alpha = 5$. Even more, there is a change of sign for $n = 3$ and $n = 4$. The same oscillatory behaviour is observed for $L = 3, 4, 5, 6$ and $n = 2, 3, 4$. However, for $L = 7, 8, 9, 10$ the function increases monotonously up to a certain $\alpha \approx 5$ where the frequency reaches a maximum and then decreases and converges to a certain constant value. It is worth mentioning that it is

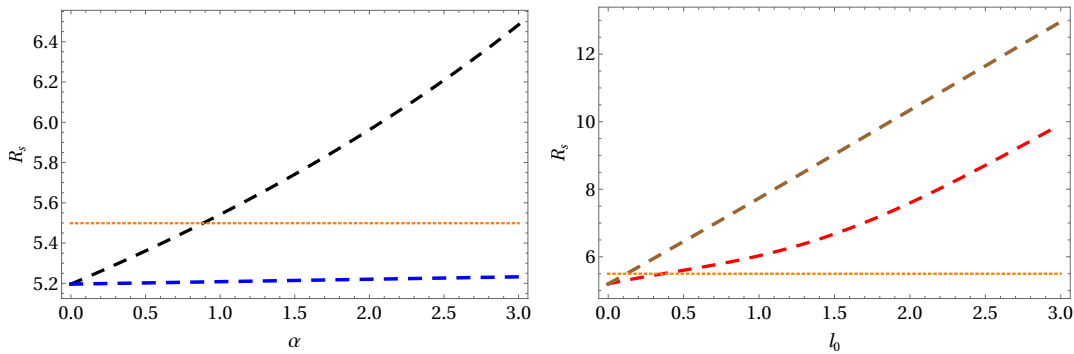


Fig. 1 Typical radius of the shadow, \mathcal{R}_s as function of α for models 1 (black line) and 2 (blue line) in the left panel and as a function of ℓ_0 for model 3 (red line) and 4 (brown line) in the right panel. The horizontal orange line corresponds to $\mathcal{R}_s = 5.49874$ for M87 BH as discussed in the text.

claimed that the method has high accuracy for small n and large L so that, the change of sign for $n = 3, 4$ for $L = 2$ could be associated with the lack of precision for the values under study and not to instabilities of the BH. Similarly, we could conclude that the oscillatory behavior is a result of the low precision of the method for large n and small L . Finally, the damping of the signal given by $e^{-i\text{Im}(\omega)}$, decreases as α grows (except in the oscillatory interval). Accordingly, as α increases, the oscillation dominates at late times. Furthermore, the frequency of the the oscillations (the $\text{Re}(\omega)$) decreases when α increases as shown in Tables 1, 2, and 3. Also, we note that as α takes bigger values, the $\text{Re}(\omega)$ converges to the same values for the different overtones n and a fixed L . In summary, as the parameter associated with the primary hair increases the signal becomes less damped and the dominant oscillatory behavior at late times becomes “monochromatic” for each multipole number L .

In Fig 3 we show the results for Model 2. Note that for $L = 2$ the frequency remains constant for $n = 0, 1, 2$. Besides, the value of the frequency decreases as n increases. For $n = 3, 4$ the frequency is a decreasing function and undergoes an oscillatory behavior around $\alpha \approx 10$. In contrast, for $L = 3, 4, 5, 6, 7, 8$, $\text{Im}(\omega)$ is constant for $n = 0, 1, 2$ but a maximum around $\alpha \approx 0$ for $n = 3, 4$. For $L = 9, 10$ the frequency is almost constant for every value of the overtone under consideration. However, in contrast to what occurs in Model 1, the values of $\text{Re}(\omega)$ are different for a fixed multiple number L and different overtones n . Even more, their separation increase as the primary hair grows as shown in tables 1, 2, and 3. In any case, the results indicate that Model 2 is stable for all the values of the hair considered here. Based on these results, we conclude that for this model, the damping of the signal is almost the same for each value of the primary hair but the fre-

quency of oscillations at late times depends critically on the value of α .

The results for Model 3 are shown in Fig. 4. We note that, except for $L = 2, 3$ where there is an oscillatory behavior for $n = 3, 4$, the frequency increases monotonously. Besides, $\text{Im}(\omega)$ is always negative indicating that this model is stable for each value of the primary hair under consideration. Again, as in Model 1, both the damping of the signal and $\text{Re}(\omega)$ decreases as α grows (except in the oscillatory interval)

In Fig. 5 we show the frequency for Model 4. The behavior is similar to that seen in Models 1 and 3. The only difference is that, in this case, there is not any oscillatory behavior for any values of n or L .

Another point that deserves discussion is the values taken by $\text{Im}(\omega)$ for a fixed multipole, L , and different values of the overtone n . A well-established point is that for a fixed L , the absolute value of the imaginary part of the QNM frequency increases as n grows [1, 20]. This behavior is shown by Models 2, 3, and 4 for all the values of the primary hairs under consideration. In this regard, as n increases, the damping is strong. In Model 1, the oscillatory behavior for $L = 2, 3$ and $n = 3, 4$ violates this tendency for a certain value of α but as we stated before this should be related to the lack of accuracy of the method.

In summary, we conclude that the role played by the primary hair in the BH is twofold: to modulate the damping factor of the perturbation and to decrease the frequency of the dominant oscillations at late times.

Before concluding this section we would like to emphasize that the results obtained here can be matched with observational data thorough the relationship between the real part of the QNM and the the typical radius of the shadow \mathcal{R}_s . Indeed, in Ref. [83] the authors found a relationship between the QNM frequencies and the metric evaluated at the radius of the photon sphere at third order WKB. It should be interesting to explore

this relationship to higher orders with the aim to apply this results with the finding here. However, this issue is out the scope of this paper and could be explore in a future work.

5 Conclusion

In this work, we computed the frequencies of the quasinormal modes through the 13th order WKB approach of four models of hairy black holes. All the results were shown as a function of the primary hair parameter of the black holes. All the plots were made by varying the values of the primary hair parameters in a step of 0.1 in $\alpha, \ell_0 \in (-50, 50)$. However, in this work we only showed the results for $\alpha, \ell_0 \in (-10, 10)$ given that such an interval contains all the information we required for the discussion. We found that (except for some multipole parameters in Model 1) all the black holes are stable under the perturbation for the values under consideration in the sense that the imaginary part of the quasinormal mode frequencies is always negative. Besides, we obtained that for a fixed value of the multipole parameter an increase of the overtone leads to an increase of both the absolute value of the imaginary part real part of the quasinormal modes. This result shows that, at a late time, the dominant oscillatory behavior is that with the least frequency. Regarding the effect that the primary hair has on the perturbation, we found that in Models 1, 3, and 4, the damping factor diminishes as the parameter associated with the hair grows. However, for Model 2 the frequencies are almost constant so that, in this case, the primary hair has no effect on the stability of the black hole geometry.

Acknowledgments

EC is suported by Polygrant N° 17459. The authors acknowledge Roman Konoplya for fruitful exchange of correspondence and for providing us the script for the computation of the QNM at 13th order.

References

1. R. A. Konoplya and A. Zhidenko. Quasinormal modes of black holes: From astrophysics to string theory. *Rev. Mod. Phys.*, 83:793–836, 2011.
2. R. A. Konoplya and A. Zhidenko. Quasinormal ringing of general spherically symmetric parametrized black holes. 1 2022.
3. M. S. Churilova, R. A. Konoplya, and A. Zhidenko. Analytic formula for quasinormal modes in the near-extreme Kerr–Newman–de Sitter space-time governed by a non-Pöschl–Teller potential. *Phys. Rev. D*, 105(8):084003, 2022.
4. R. A. Konoplya, A. F. Zinhailo, and Z. Stuchlik. Quasinormal modes and Hawking radiation of black holes in cubic gravity. *Phys. Rev. D*, 102(4):044023, 2020.
5. R. A. Konoplya and A. F. Zinhailo. Quasinormal modes, stability and shadows of a black hole in the 4D Einstein–Gauss–Bonnet gravity. *Eur. Phys. J. C*, 80(11):1049, 2020.
6. Roman A. Konoplya, C. Posada, Z. Stuchlík, and A. Zhidenko. Stable Schwarzschild stars as black-hole mimickers. *Phys. Rev. D*, 100(4):044027, 2019.
7. Angel Rincon, P. A. Gonzalez, Grigoris Panotopoulos, Joel Saavedra, and Yerko Vasquez. Quasinormal modes for a non-minimally coupled scalar field in a five-dimensional Einstein-power-Maxwell background. 12 2021.
8. Grigoris Panotopoulos and Ángel Rincón. Quasinormal spectra of scale-dependent Schwarzschild–de Sitter black holes. *Phys. Dark Univ.*, 31:100743, 2021.
9. Ángel Rincón and Victor Santos. Greybody factor and quasinormal modes of Regular Black Holes. *Eur. Phys. J. C*, 80(10):910, 2020.
10. Ángel Rincón and Grigoris Panotopoulos. Quasinormal modes of an improved Schwarzschild black hole. *Phys. Dark Univ.*, 30:100639, 2020.
11. Angel Rincon and Grigoris Panotopoulos. Quasinormal modes of black holes with a scalar hair in Einstein–Maxwell–dilaton theory. *Phys. Scripta*, 95(8):085303, 2020.
12. Wei Xiong, Peng Liu, Cheng-Yong Zhang, and Chao Niu. Quasi-normal modes of the Einstein–Maxwell–aether Black Hole. 12 2021.
13. Chao Zhang, Tao Zhu, and Anzhong Wang. Gravitational axial perturbations of Schwarzschild-like black holes in dark matter halos. *Phys. Rev. D*, 104(12):124082, 2021.
14. Grigoris Panotopoulos and Ángel Rincón. Quasinormal modes of five-dimensional black holes in non-commutative geometry. *Eur. Phys. J. Plus*, 135(1):33, 2020.
15. Chong Oh Lee, Jin Young Kim, and Mu-In Park. Quasi-normal modes and stability of Einstein–Born–Infeld black holes in de Sitter space. *Eur. Phys. J. C*, 80(8):763, 2020.
16. M. S. Churilova, R. A. Konoplya, and A. Zhidenko. Arbitrarily long-lived quasinormal modes in a wormhole background. *Phys. Lett. B*, 802:135207, 2020.
17. R. Oliveira, D. M. Dantas, Victor Santos, and

		Model 1		Model 2		Model 3		Model 4	
L	n	Re ω	Im ω	Re ω	Im ω	Re ω	Im ω	Re ω	Im ω
6	0	1.17395	-0.08208	1.24877	-0.09627	1.07828	-0.06557	0.82851	-0.06307
	1	1.16863	-0.24669	1.24019	-0.28961	1.07411	-0.19699	0.82337	-0.18975
	2	1.15831	-0.41255	1.61297	-0.48535	1.06586	-0.32919	0.81332	-0.31804
7	0	1.35425	-0.08206	1.44067	-0.09625	1.24398	-0.06557	0.95578	-0.06306
	1	1.34961	-0.24654	1.43322	-0.28937	1.24036	-0.19691	0.95131	-0.18958
	2	1.34054	-0.41198	1.61297	-0.48429	1.23317	-0.32885	0.94253	-0.31731
8	0	1.53458	-0.08206	1.63259	-0.09624	1.40970	-0.06557	1.08307	-0.06305
	1	1.53047	-0.24644	1.62601	-0.28920	1.40650	-0.19687	1.07912	-0.18946
	2	1.52239	-0.41159	1.61297	-0.48358	1.40014	-0.32863	1.07133	-0.31682

Table 1 Numerical values for $Re(\omega)$ and $Im(\omega)$ for $\alpha = 1$

		Model 1		Model 2		Model 3		Model 4	
L	n	Re ω	Im ω	Re ω	Im ω	Re ω	Im ω	Re ω	Im ω
6	0	1.09141	-0.06802	1.24568	-0.09625	0.85604	-0.04576	0.62292	-0.04765
	1	1.08899	-0.20429	1.23665	-0.28954	0.85263	-0.13746	0.61892	-0.14334
	2	1.08457	-0.34119	1.21882	-0.48523	0.84579	-0.22972	0.61110	-0.24023
7	0	1.25896	-0.06801	1.43716	-0.09624	0.98766	-0.04575	0.71861	-0.04764
	1	1.25682	-0.20419	1.42932	-0.28931	0.98473	-0.13740	0.71514	-0.14321
	2	1.25282	-0.34085	1.41379	-0.48420	0.97894	-0.22943	0.70830	-0.23969
8	0	1.42654	-0.06800	1.62866	-0.09623	1.11929	-0.04575	0.81431	-0.04763
	1	1.42463	-0.20413	1.62173	-0.28916	1.11669	-0.13736	0.81125	-0.14313
	2	1.42100	-0.34063	1.60798	-0.48350	1.11151	-0.22929	0.80519	-0.23933

Table 2 Numerical values for $Re(\omega)$ and $Im(\omega)$ for $\alpha = 2$

		Model 1		Model 2		Model 3		Model 4	
L	n	Re ω	Im ω	Re ω	Im ω	Re ω	Im ω	Re ω	Im ω
6	0	1.00397	-0.05442	1.24261	-0.09624	0.65548	-0.03756	0.49957	-0.03835
	1	1.00447	-0.16356	1.23312	-0.28953	0.65348	-0.11284	0.49631	-0.11536
	2	1.00574	-0.27374	1.21432	-0.48523	0.64954	-0.18853	0.48993	-0.19333
7	0	1.15798	-0.05439	1.43368	-0.09624	0.75619	-0.03756	0.57632	-0.03834
	1	1.15839	-0.16340	1.42545	-0.28932	0.75445	-0.11279	0.57348	-0.11526
	2	1.15941	-0.27313	1.40909	-0.48421	0.75102	-0.18834	0.56791	-0.19290
8	0	1.31204	-0.05438	1.62476	-0.09623	0.85692	-0.03756	0.65308	-0.03834
	1	1.31238	-0.16330	1.61749	-0.28917	0.85538	-0.11276	0.65057	-0.11520
	2	1.31322	-0.27275	1.60303	-0.48353	0.85235	-0.18820	0.64563	-0.19262

Table 3 Numerical values for $Re(\omega)$ and $Im(\omega)$ for $\alpha = 3$

- C. A. S. Almeida. Quasinormal modes of bumblebee wormhole. *Class. Quant. Grav.*, 36(10):105013, 2019.
18. Grigoris Panotopoulos and Ángel Rincón. Quasinormal modes of black holes in Einstein-power-Maxwell theory. *Int. J. Mod. Phys. D*, 27(03):1850034, 2017.
19. R. A. Konoplya, A. Zhidenko, and A. F. Zinhailo. Higher order WKB formula for quasinormal modes and grey-body factors: recipes for quick and accurate calculations. *Class. Quant. Grav.*, 36:155002, 2019.
20. R. A. Konoplya. How to tell the shape of a wormhole by its quasinormal modes. *Phys. Lett. B*, 784:43–49, 2018.
21. J. Ovalle, R. Casadio, E. Contreras, and A. Sotomayor. Hairy black holes by gravitational decoupling. *Phys. Dark Univ.*, 31:100744, 2021.
22. R. T. Cavalcanti, R. C. de Paiva, and R. da Rocha. Echoes of the gravitational decoupling: scalar perturbations and quasinormal modes of hairy black holes. *Eur. Phys. J. Plus*, 137(10):1185, 2022.
23. Yi Yang, Dong Liu, Ali Övgün, Zheng-Wen Long, and Zhaoyi Xu. Probing hairy black holes caused by gravitational decoupling using quasinormal modes, and greybody bounds. 3 2022.
24. Bernard F. Schutz and Clifford M. Will. BLACK HOLE NORMAL MODES: A SEMIANALYTIC

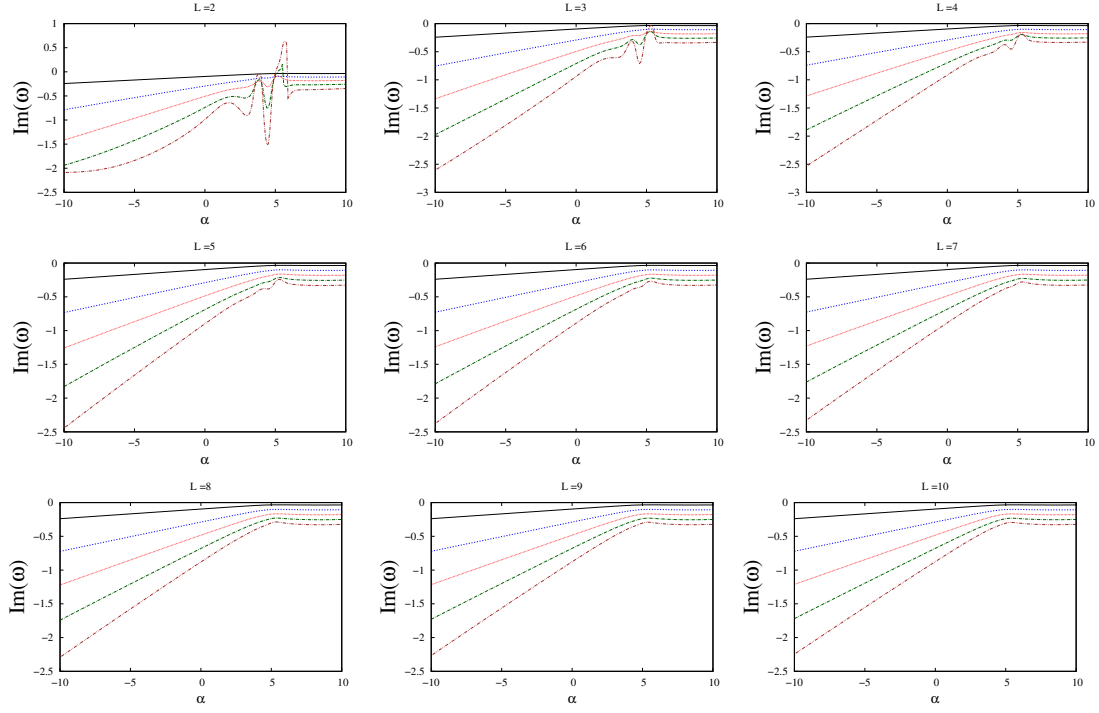


Fig. 2 Imaginary part of the QNM for Model 1 as a function of the hair α for different values of L and n . Each plot corresponds to a different value of L . The values for n are 0 (black line), 1 (blue line), 2 (red line), 3 (green line), 4 (brown line).

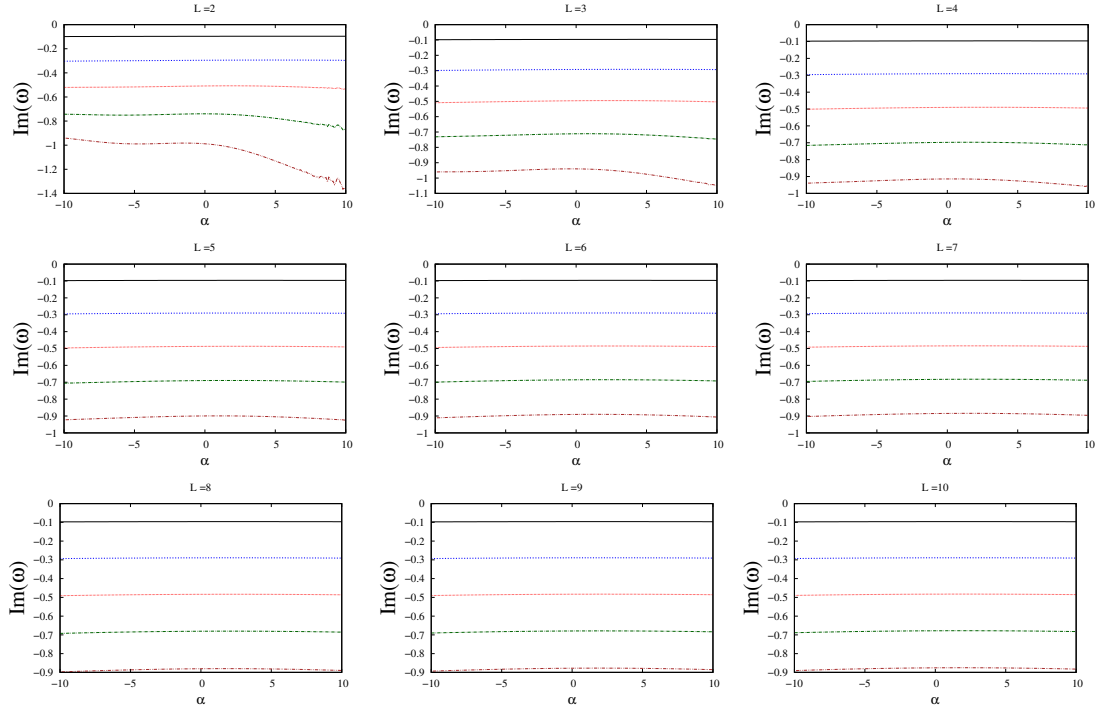


Fig. 3 Imaginary part of the QNM for Model 2 as a function of the hair α for different values of L and n . Each plot corresponds to a different value of L . The values for n are 0 (black line), 1 (blue line), 2 (red line), 3 (green line), 4 (brown line).

APPROACH. *Astrophys. J. Lett.*, 291:L33–L36, 1985.

25. C. Las Heras and P. Leon. Complexity factor of spherically anisotropic polytropes from gravita-

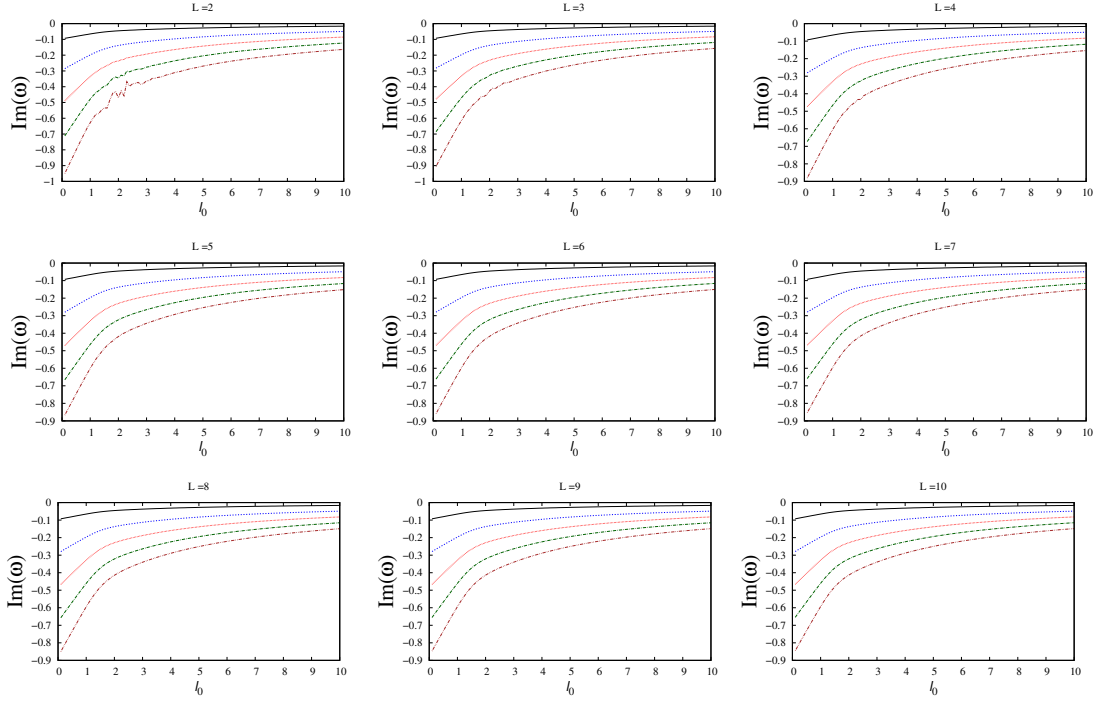


Fig. 4 Imaginary part of the QNM for Model 3 as a function of the hair α for different values of L and n . Each plot corresponds to a different value of L . The values for n are 0 (black line), 1 (blue line), 2 (red line), 3 (green line), 4 (brown line).

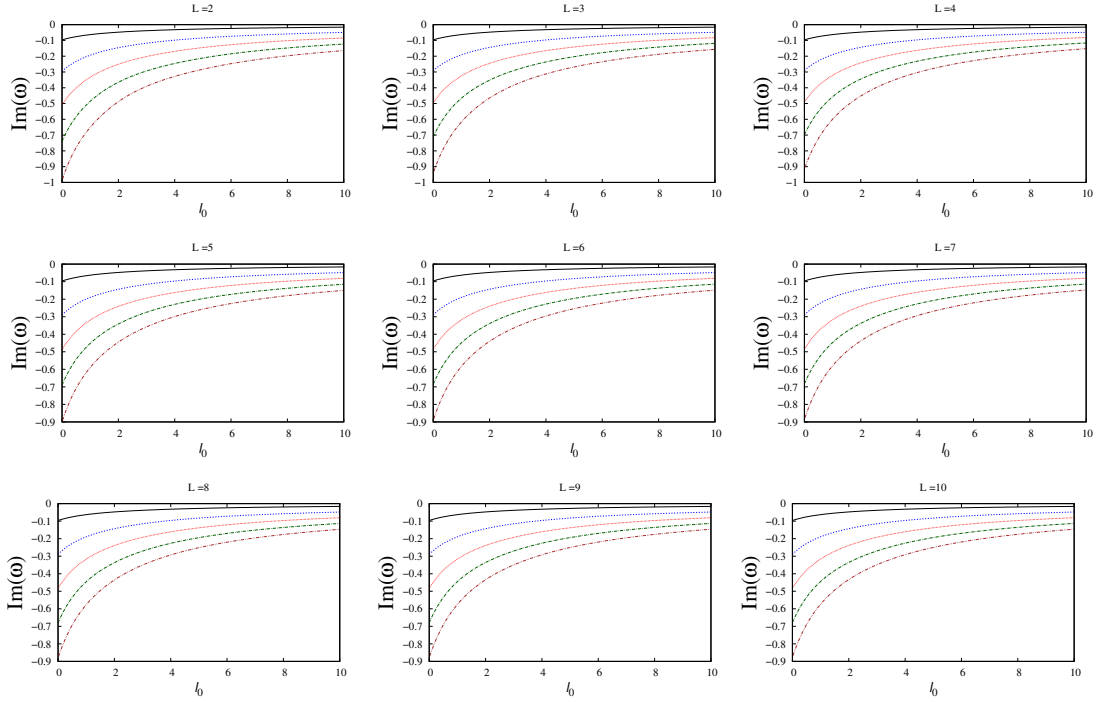


Fig. 5 Imaginary part of the QNM for Model 4 as a function of the hair α for different values of L and n . Each plot corresponds to a different value of L . The values for n are 0 (black line), 1 (blue line), 2 (red line), 3 (green line), 4 (brown line).

27. Hina Azmat, M. Zubair, and Zahid Ahmad. Study of anisotropic and non-uniform Gravastars by gravitational decoupling in $f(R,T)$ gravity. *Annals Phys.*, 439:168769, 2022.
28. S. K. Maurya, M. Govender, Ksh. Newton Singh, and Riju Nag. Gravitationally decoupled anisotropic solution using polytropic EoS in the framework of 5D Einstein–Gauss–Bonnet Gravity. *Eur. Phys. J. C*, 82(1):49, 2022.
29. J. Andrade. Stellar solutions with zero complexity obtained through a temporal metric deformation. *Eur. Phys. J. C*, 82:266, 2022.
30. J. Ovalle, E. Contreras, and Z. Stuchlik. Energy exchange between relativistic fluids: the polytropic case. *Eur. Phys. J. C*, 82(3):211, 2022.
31. J. Ovalle. Warped vacuum energy by black holes. *Eur. Phys. J. C*, 82(2):170, 2022.
32. S. K. Maurya and Riju Nag. Role of gravitational decoupling on isotropization and complexity of self-gravitating system under complete geometric deformation approach. *Eur. Phys. J. C*, 82(1):48, 2022.
33. M. Zubair, Hina Azmat, and Mubeen Amin. Charged anisotropic fluid sphere in comparison with its uncharged analogue through extended geometric deformation. *Chin. J. Phys.*, 77:898–914, 2022.
34. Roldao da Rocha. Gravitational decoupling of generalized Horndeski hybrid stars. *Eur. Phys. J. C*, 82(1):34, 2022.
35. Hina Azmat and M. Zubair. Anisotropic counterpart of charged Durgapal V perfect fluid sphere. *Int. J. Mod. Phys. D*, 30(15):2150115, 2021.
36. S. K. Maurya, Anirudh Pradhan, Francisco Tello-Ortiz, Ayan Banerjee, and Riju Nag. Minimally deformed anisotropic stars by gravitational decoupling in Einstein–Gauss–Bonnet gravity. *Eur. Phys. J. C*, 81(9):848, 2021.
37. Roldao da Rocha. MGD Dirac stars. *Symmetry*, 12(4):508, 2020.
38. Pedro Meert and Roldao da Rocha. Gravitational decoupling, hairy black holes and conformal anomalies. *Eur. Phys. J. C*, 82(2):175, 2022.
39. Joseph Sultana. Gravitational Decoupling in Higher Order Theories. *Symmetry*, 13(9):1598, 2021.
40. Francisco Tello-Ortiz, S. K. Maurya, and Pedro Bargueño. Minimally deformed wormholes. *Eur. Phys. J. C*, 81(5):426, 2021.
41. S. K. Maurya, Francisco Tello-Ortiz, and Saibal Ray. Decoupling gravitational sources in $f(R,T)$ gravity under class I spacetime. *Phys. Dark Univ.*, 31:100753, 2021.
42. Roldao da Rocha. Minimal geometric deformation of Yang-Mills-Dirac stellar configurations. *Phys. Rev. D*, 102(2):024011, 2020.
43. Francisco Tello-Ortiz, S.K. Maurya, and Y. Gomez-Leyton. Class I approach as MGD generator. *Eur. Phys. J. C*, 80(4):324, 2020.
44. Jorge Ovalle and Roberto Casadio. *Beyond Einstein Gravity*. SpringerBriefs in Physics. Springer Nature, Cham, 2020.
45. Roldao da Rocha and Anderson A. Tomaz. MGD-decoupled black holes, anisotropic fluids and holographic entanglement entropy. *Eur. Phys. J. C*, 80:857, 2020.
46. P. Meert and R. da Rocha. Probing the minimal geometric deformation with trace and Weyl anomalies. *Nucl. Phys. B*, 967:115420, 2021.
47. Francisco Tello-Ortiz. Minimally deformed anisotropic dark stars in the framework of gravitational decoupling. *Eur. Phys. J. C*, 80(5):413, 2020.
48. S.K. Maurya. Extended gravitational decoupling (GD) solution for charged compact star model. *Eur. Phys. J. C*, 80(5):429, 2020.
49. S.K. Maurya, Ksh. Newton Singh, and B. Dayanandan. Non-singular solution for anisotropic model by gravitational decoupling in the framework of complete geometric deformation (CGD). *Eur. Phys. J. C*, 80(5):448, 2020.
50. J. Ovalle. Decoupling gravitational sources in general relativity: The extended case. *Phys. Lett.*, B788:213–218, 2019.
51. R. Da Rocha and Anderson A. Tomaz. Holographic entanglement entropy under the minimal geometric deformation and extensions. *Eur. Phys. J. C*, 79(12):1035, 2019.
52. Camilo Las Heras and Pablo León. New algorithms to obtain analytical solutions of Einstein’s equations in isotropic coordinates. *Eur. Phys. J. C*, 79(12):990, 2019.
53. S.K. Maurya and Francisco Tello-Ortiz. Generalized relativistic anisotropic compact star models by gravitational decoupling. *Eur. Phys. J. C*, 79(1):85, 2019.
54. L. Gabbanelli, J. Ovalle, A. Sotomayor, Z. Stuchlik, and R. Casadio. A causal Schwarzschild-de Sitter interior solution by gravitational decoupling. *Eur. Phys. J. C*, 79(6):486, 2019.
55. Milko Estrada. A way of decoupling gravitational sources in pure Lovelock gravity. *Eur. Phys. J. C*, 79(11):918, 2019.
56. J. Ovalle, C. Posada, and Z. Stuchlik. Anisotropic ultracompact Schwarzschild star by gravitational decoupling. *Class. Quant. Grav.*, 36(20):205010, 2019.

57. S.K. Maurya and Francisco Tello-Ortiz. Charged anisotropic compact star in $f(R, T)$ gravity: A minimal geometric deformation gravitational decoupling approach. *Phys. Dark Univ.*, 27:100442, 2020.
58. Sudipta Hensh and Zdenek Stuchlík. Anisotropic Tolman VII solution by gravitational decoupling. *Eur. Phys. J. C*, 79(10):834, 2019.
59. A. Fernandes-Silva, A. J. Ferreira-Martins, and R. da Rocha. Extended quantum portrait of MGD black holes and information entropy. *Phys. Lett.*, B791:323–330, 2019.
60. P. Leon and A. Sotomayor. Braneworld Gravity under gravitational decoupling. *Fortsch. Phys.*, 67(12):1900077, 2019.
61. Ksh.Newton Singh, S.K. Maurya, M.K. Jasim, and Farook Rahaman. Minimally deformed anisotropic model of class one space-time by gravitational decoupling. *Eur. Phys. J. C*, 79(10):851, 2019.
62. S.K. Maurya. A completely deformed anisotropic class one solution for charged compact star: a gravitational decoupling approach. *Eur. Phys. J. C*, 79(11):958, 2019.
63. L. Gabbanelli, A. Rincón, and C. Rubio. Gravitational decoupled anisotropies in compact stars. *Eur. Phys. J.*, C78(5):370, 2018.
64. J. Ovalle, R. Casadio, R. da Rocha, A. Sotomayor, and Z. Stuchlík. Black holes by gravitational decoupling. *Eur. Phys. J.*, C78(11):960, 2018.
65. A. Fernandes-Silva, A. J. Ferreira-Martins, and R. Da Rocha. The extended minimal geometric deformation of $SU(N)$ dark glueball condensates. *Eur. Phys. J.*, C78(8):631, 2018.
66. E. Morales and Francisco Tello-Ortiz. Charged anisotropic compact objects by gravitational decoupling. *Eur. Phys. J. C*, 78(8):618, 2018.
67. Milko Estrada and Francisco Tello-Ortiz. A new family of analytical anisotropic solutions by gravitational decoupling. *Eur. Phys. J. Plus*, 133(11):453, 2018.
68. C. Las Heras and P. Leon. Using MGD gravitational decoupling to extend the isotropic solutions of Einstein equations to the anisotropical domain. *Fortsch. Phys.*, 66(7):1800036, 2018.
69. G. Panotopoulos and A. Rincón. Minimal Geometric Deformation in a cloud of strings. *Eur. Phys. J.*, C78(10):851, 2018.
70. E. Morales and Francisco Tello-Ortiz. Compact Anisotropic Models in General Relativity by Gravitational Decoupling. *Eur. Phys. J. C*, 78(10):841, 2018.
71. Milko Estrada and Reginaldo Prado. The Gravitational decoupling method: the higher dimensional case to find new analytic solutions. *Eur. Phys. J. Plus*, 134(4):168, 2019.
72. J. Ovalle, R. Casadio, R. da Rocha, A. Sotomayor, and Z. Stuchlík. Einstein-Klein-Gordon system by gravitational decoupling. *EPL*, 124(2):20004, 2018.
73. J. Ovalle, R. Casadio, R. da Rocha, and A. Sotomayor. Anisotropic solutions by gravitational decoupling. *Eur. Phys. J.*, C78(2):122, 2018.
74. Jorge Ovalle. Decoupling gravitational sources in general relativity: from perfect to anisotropic fluids. *Phys. Rev.*, D95(10):104019, 2017.
75. A. Ramos, C. Arias, R. Avalos, and E. Contreras. Geodesic motion around hairy black holes. *Annals Phys.*, 431:168557, 2021.
76. G. Risaliti et al. Variable partial covering and a relativistic iron line in NGC 1365. *Astrophys. J.*, 696:160–171, 2009.
77. G. Risaliti et al. A rapidly spinning supermassive black hole at the centre of NGC 1365. *Nature*, 494:449, 2013.
78. L. W. Brenneman, G. Risaliti, M. Elvis, and E. Nardini. An Examination of the Spectral Variability in NGC 1365 with Suzaku. *Mon. Not. Roy. Astron. Soc.*, 429:2662, 2013.
79. E. Contreras, J. Ovalle, and R. Casadio. Gravitational decoupling for axially symmetric systems and rotating black holes. *Phys. Rev. D*, 103(4):044020, 2021.
80. Kimet Jusufi, Mustapha Azreg-Aïnou, Mubasher Jamil, Shao-Wen Wei, Qiang Wu, and Anzhong Wang. Quasinormal modes, quasiperiodic oscillations, and the shadow of rotating regular black holes in nonminimally coupled Einstein-Yang-Mills theory. *Phys. Rev. D*, 103(2):024013, 2021.
81. Kimet Jusufi. Quasinormal Modes of Black Holes Surrounded by Dark Matter and Their Connection with the Shadow Radius. *Phys. Rev. D*, 101(8):084055, 2020.
82. Kimet Jusufi. Connection Between the Shadow Radius and Quasinormal Modes in Rotating Spacetimes. *Phys. Rev. D*, 101(12):124063, 2020.
83. B. Cuadros-Melgar, R. D. B. Fontana, and Jefferson de Oliveira. Analytical correspondence between shadow radius and black hole quasinormal frequencies. *Phys. Lett. B*, 811:135966, 2020.